

# Crystalline Structure and Vacancy Ordering across a Surface Phase Transition in Sn/Cu(001)

J. Martínez-Blanco,<sup>†</sup> V. Joco,<sup>†</sup> C. Quirós,<sup>‡,¶</sup> P. Segovia,<sup>†,§,||</sup> and E.G.  
Michel<sup>\*,†,§,||</sup>

<sup>†</sup>*Departamento de Física de la Materia Condensada, Universidad Autónoma de Madrid, 28049,  
Madrid, Spain*

<sup>‡</sup>*Departamento de Física, Universidad de Oviedo, 33007 Oviedo, Spain*

<sup>¶</sup>*Centro de Investigación en Nanomateriales y Nanotecnología, CINN (CSIC – Universidad de  
Oviedo), 33940 El Entrego, Spain.*

<sup>§</sup>*Condensed Matter Physics Center (IFIMAC), Universidad Autónoma de Madrid, 28049 Madrid,  
Spain*

<sup>||</sup>*Instituto Universitario de Ciencia de Materiales “Nicolás Cabrera”, Universidad Autónoma de  
Madrid, 28049 Madrid, Spain*

E-mail: [enrique.garcia.michel@uam.es](mailto:enrique.garcia.michel@uam.es)

## Abstract

We report a surface x-ray diffraction study of the crystalline structure changes and critical behavior across the  $(3\sqrt{2} \times \sqrt{2})R45^\circ \rightarrow (\sqrt{2} \times \sqrt{2})R45^\circ$  surface phase transition at 360 K for 0.5 monolayers of Sn on Cu(100). The phase transition is of the order-disorder type and is due to the disordering of the Cu atomic vacancies present in the low temperature phase. Two different atomic sites for Sn atoms, characterized by two different heights, are maintained across the surface phase transition.

## Introduction

A broad range of novel and interesting physical phenomena take place at the surfaces and interfaces of solids. Many of them are related to the appearance of surface or interface phases, as a consequence of a surface phase transition. Critical phenomena at surfaces often present specific features, like surface critical exponents<sup>1,2</sup> or critical temperatures different from the bulk<sup>3</sup>. Phase transitions with surface specific properties include structural transformations of the top atomic layers of a crystal (surface reconstruction)<sup>1</sup>, surface melting<sup>4</sup>, enrichment of one component at the surface of a solid binary alloy (surface segregation)<sup>1</sup>, sophisticated phenomena related to self-organization, like the ordering of atom vacancies into line defects or vacancy line superstructures<sup>5-7</sup>, specific kinetics for Under Potential Deposition conditions<sup>8</sup>, and structural transformations of organic ultrathin films<sup>9</sup> or metallic layers<sup>10</sup>. Other examples include magnetically ordered systems, with a surface Curie temperature different from the bulk<sup>11</sup>, Mott<sup>12</sup> or Wigner-Mott transition<sup>13</sup>, or collective states, including superconductivity<sup>14,15</sup>, and charge density waves (CDWs)<sup>16-21</sup>. In last years, CDW phase transitions have been reported for different metals on the (100) faces of noble metals, notably Cu(100), including In<sup>20</sup>, Tl<sup>22</sup>, Sn<sup>21</sup>, Bi<sup>23,24</sup>, and Pb<sup>25</sup>. In general, these phase transitions involve a periodic lattice distortion with a complex lattice at low temperature, with general structure  $(m\sqrt{2} \times n\sqrt{2})R45^\circ$ , where  $m$  and  $n$  are integer numbers, and frequently a simpler  $(\sqrt{2} \times \sqrt{2})R45^\circ$  ( $c(2 \times 2)$ ) structure above the phase transition. The structure of the low temperature phase can be both primitive or centred<sup>26,27</sup>. The critical temperature is in most cases near

or slightly above room temperature. An electronic phase transition, with gap opening and partial Fermi surface nesting takes place simultaneously, but not necessarily exactly at the same time with the structural phase transition<sup>21,27</sup>. A specific feature of this family of phase transitions, besides the concomitant observation of structural and electronic changes, typical of a CDW, is a large band gap (in range of 100 meV), observed only in small regions of reciprocal space. This is indicative of a strong electron-phonon coupling, simultaneous with a large electronic coherence length<sup>26,27</sup>. A strong coupling is usually associated with the order-disorder character of the high temperature phase<sup>16</sup>. Recent investigations in Sn/Cu(100) have indeed identified that the atomistic mechanism behind the structural phase transition is an order/disorder transition driven by the Cu vacancy entropy<sup>28</sup>.

There are five different surface phases for submonolayers of Sn deposited on Cu(100) at room temperature<sup>29-36</sup>:  $p(2 \times 2)$  at 0.21 ML,  $p(2 \times 6)$  at 0.33 ML with two rotational domains,  $\begin{pmatrix} -4 & 2 \\ 0 & 4 \end{pmatrix}$  (equivalent to  $c(4 \times 8)$ ) at  $\sim 0.40-0.45$  ML,  $(3\sqrt{2} \times \sqrt{2}) R45^\circ$  at 0.5 ML, and  $(2\sqrt{2} \times 2\sqrt{2}) R45^\circ$  (equivalent to  $c(4 \times 4)$ ) at 0.65 ML.

Sn/Cu(100) surface phases have received a renewed attention since the discovery of the phase transition  $(3\sqrt{2} \times \sqrt{2}) R45^\circ \rightarrow (\sqrt{2} \times \sqrt{2}) R45^\circ$ <sup>21,37</sup>. Similar phase transitions have been observed in the case of two surface phases of In/Cu(100)<sup>20,38</sup> and for other surface phases of Sn/Cu(100)<sup>34,39</sup>. The ground state of these surface phases has been interpreted as a surface charge density wave<sup>20,21,26,27,37,38</sup>. The relevance of order-disorder effects has been highlighted in several papers<sup>28,40</sup>.

The Sn/Cu(001)- $(3\sqrt{2} \times \sqrt{2}) R45^\circ$  low-temperature phase is described as a layer of 0.5 ML of Sn atoms occupying the hollow sites of the top Cu(001) atomic layer (see Fig. 1). Sn atoms are intermixed with Cu atoms, and the layer is properly described as an alloy. The 3-fold periodicity is in fact due to a missing row of Cu atoms (corresponding to 1/3 of a monolayer, ML) of the top mixed layer. Due to the missing Cu row, nearest neighbor Sn atoms get closer and deeper than Sn atoms that are not near the missing Cu row. As a result, the whole surface is rippled with 3-fold periodicity, and when viewed with Scanning Tunneling Microscopy (STM), it is

seen as a succession of higher and deeper stripes<sup>28</sup>. The atomic positions of this structure have been described with great accuracy using low-energy electron diffraction (LEED)<sup>33</sup>, surface x-ray diffraction (SXRD)<sup>41</sup>, helium atom scattering<sup>36</sup> and ion scattering<sup>42</sup>. Concomitantly to the structural phase transition, electronic changes take place. We refer the reader to previous papers for a full account on the electronic properties<sup>21,37,43</sup>.

A detailed analysis of the crystalline structure of the  $(3\sqrt{2} \times \sqrt{2}) R45^\circ$  phase has been made before using dynamic LEED<sup>33</sup> and SXRD<sup>41</sup>. We summarize here its most important features and refer the reader to previous works<sup>33,41</sup> for more details. The structure found is a substitutional surface alloy. Sn atoms in the last layer substitute Cu atoms occupying  $(\sqrt{2} \times \sqrt{2}) R45^\circ$  positions. The  $(3\sqrt{2} \times \sqrt{2}) R45^\circ$  periodicity is due to formation of pairs of Sn atoms by two out of the three atoms in the unit cell, which get closer to each other, while the third Sn atom occupies a higher position. The atomic row of Cu atoms between the paired Sn atoms (one out of three in the surface) is removed, so that the reconstruction is of the “missing row” type. Additional support to this model has come from MEIS (medium energy ion scattering) results<sup>42</sup>.

In this paper we report a surface x-ray diffraction (SXRD) study on the structure of the Sn/Cu(001)- $(\sqrt{2} \times \sqrt{2}) R45^\circ$  high temperature phase and on the critical behavior of the phase transition at 360 K into a  $(3\sqrt{2} \times \sqrt{2}) R45^\circ$  low temperature phase. We find that the phase transition is of the order-disorder type, and determine the origin and properties of the atomic disorder observed, which we ascribe to the mobility of Cu vacancies present in the low temperature phase. An increase of Cu density in the topmost atomic layer is an additional mechanism of the phase transition. The local crystalline environment around Sn atoms is similar to the low temperature phase.

## Experiment

The experiments are performed at the ID03 beamline of the European Synchrotron Radiation Facility (E.S.R.F) in Grenoble, France. The sample is cleaned by repeated cycles of ion sputtering and annealing to 900 K. Surface cleanliness is checked by Auger Electron Spectroscopy, while the

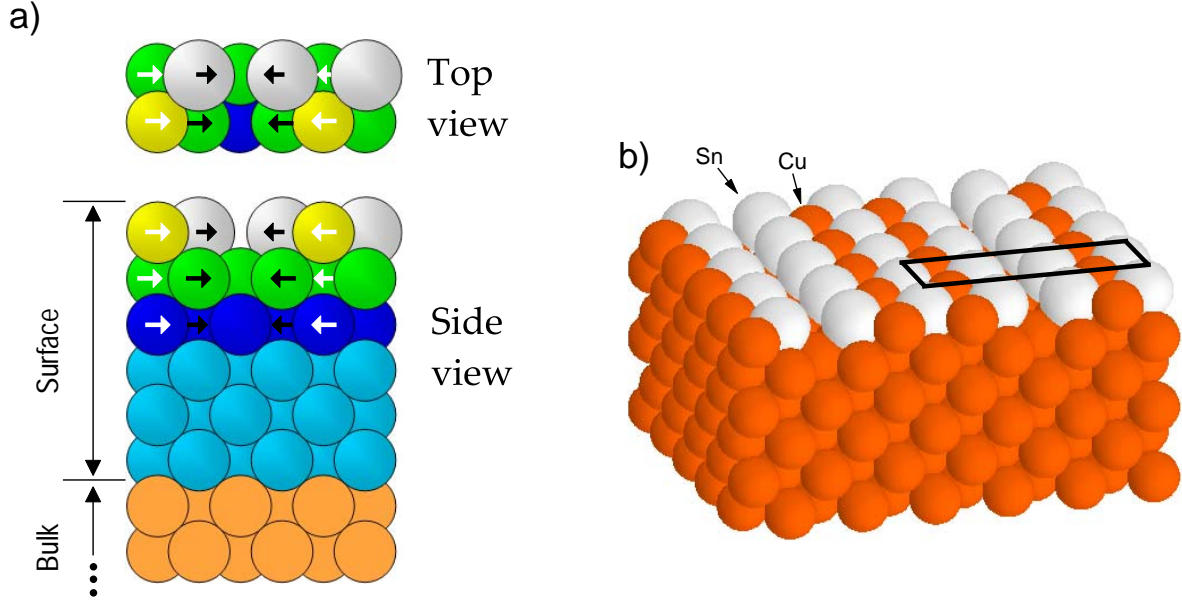


Figure 1: Structure of the  $(3\sqrt{2} \times \sqrt{2})R45^\circ$  low temperature phase (a) Top and side views of the unit cell, showing the surface and bulk layers. White circles correspond to Sn atoms, all other circles are Cu atoms of the top layer (yellow), second layer (green), third layer (blue), other surface layers (cyan) and bulk (orange). Arrows indicate the directions of displacements in the reconstruction. Note the missing Cu row in the first layer (yellow). (b) 3D perspective of the unit cell repeated several times. A rectangle highlights the surface unit cell.

crystalline quality of the surface is determined from the terrace size, estimated from the width in reciprocal space of x-ray reflections<sup>44</sup>, providing a mean Cu(100) terrace size of 900 Å. The sample temperature is measured with a thermocouple in contact with the sample holder. The coverage is calibrated from the sequence of structures below 1 ML<sup>34</sup> and by monitoring the intensity of reconstruction-related x-ray reflections. The Sn/Cu(001)- $(3\sqrt{2} \times \sqrt{2})R45^\circ$  phase is formed after depositing 0.5 ML of Sn from a Knudsen cell onto a Cu(001) surface at 300 K. The temperature induced phase transition into the Sn/Cu(001)- $(\sqrt{2} \times \sqrt{2})R45^\circ$  is fully reversible and is observed at 360 K. The average domain size of the  $(3\sqrt{2} \times \sqrt{2})R45^\circ$  phase is 480 Å, estimated from the width of the  $(\frac{5}{6}, \frac{5}{6})$  reconstruction x-ray reflection. This value is achieved after cycling several times across the phase transition (the average domain size is only 280 Å right after depositing Sn). The average domain size of the high temperature  $(\sqrt{2} \times \sqrt{2})R45^\circ$  phase is 1280 Å, measured from the width of the  $(\frac{1}{2}, \frac{1}{2})$  reconstruction x-ray reflection at 470 K. This value is even larger than the

terrace size of the clean Cu(001) surface, suggesting that Sn deposition improves the long range order at the surface.

The experimental data were treated following standard procedures to obtain the normalized integrated intensity, taking into account the correction derived from the diffractometer geometry. The development and refinement of the structural model found was made using the code ORUGA (Obtaining Rods Using Genetic Algorithm), which is inspired by ROD code<sup>45</sup> and makes use of a differential evolution algorithm to optimize the structure. The algorithm has demonstrated to be very efficient, both by the speed to find the minimum of the error functions, and by the reproducibility of the results, which is a proof of its ability to overcome local minima. To the best of our knowledge, the method has not been applied so far to solve a problem like the one considered in this paper. However, a previous use of the genetic algorithm to solve the structure of the low temperature phase<sup>41</sup> provided structural parameters in excellent agreement with previous studies using other techniques, what gives confidence in the suitability of the method and in its capacity to obtain crystallographic parameters from SXRD data. Most of the information is obtained using simultaneously the full experimental data set, and the method is able to work very well, even in the case of many fitted parameters. We refer the reader to Ref. 41 for more details on the data treatment and on the ORUGA code.

## Results

The crucial point to determine the nature of the high temperature phase and of the temperature induced phase transition is to find out both the in-plane and the out-of-plane distortions reliably. To this end, we took in-plane and out-of-plane measurements, probing extensive portions of the reciprocal space.

## Structural phase transition

Fig.2(a) and (b) show the LEED patterns for the low temperature and high temperature phases. SXRD is used to measure with high resolution the  $(\frac{5}{6}, \frac{5}{6})$  x-ray reflection of the low temperature phase as a function of temperature. Panel (c) (left axis) shows the dependence with temperature of the intensity of this x-ray reflection, measured with 17.119 keV for a low perpendicular momentum transfer ( $l = 0.2$ ), corresponding to a light incidence angle on the sample of  $1^\circ$ . Panel c) (right axis) shows the evolution of the full widths at half maximum (FWHM) of the x-ray reflection. Above  $T_c$ , the diffraction peaks are broadened, revealing a reduction of the  $(3\sqrt{2} \times \sqrt{2}) R45^\circ$  domains below  $40 \text{ \AA}$  at  $\sim 400 \text{ K}$ .

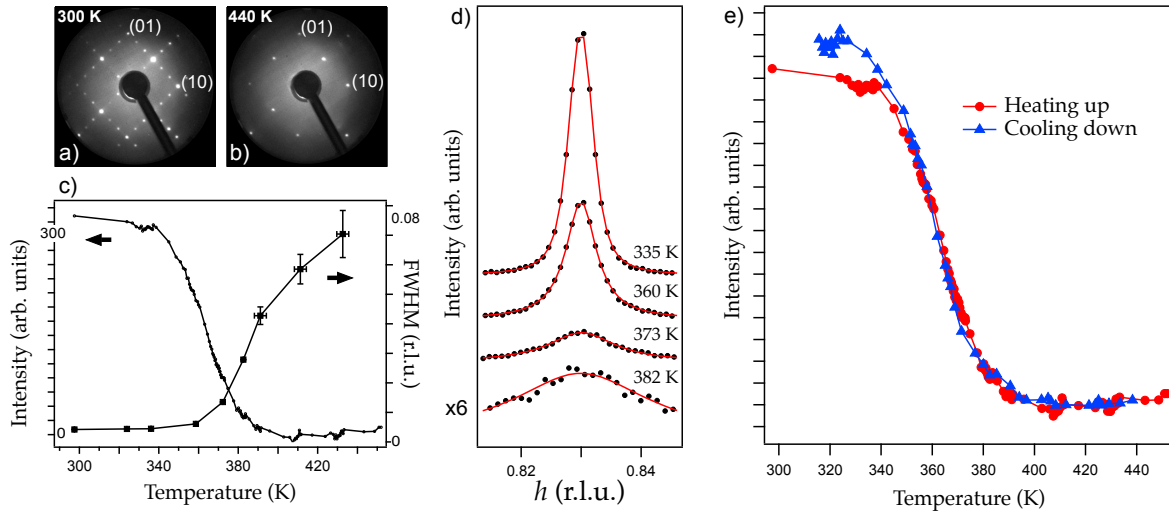


Figure 2: LEED patterns at 70 eV primary energy for the  $(3\sqrt{2} \times \sqrt{2})R45^\circ$  (a) and the  $(\sqrt{2} \times \sqrt{2})R45^\circ$  (b) phases. c) Integrated intensity and peak width of the surface x-ray reflection  $(\frac{5}{6}, \frac{5}{6})$  (specific of the  $(3\sqrt{2} \times \sqrt{2})R45^\circ$ ) vs. temperature. The peak line shape is shown for some selected temperatures in panel d), fitted to a Voigt line shape (red line). e) Integrated intensity of the  $(\frac{5}{6}, \frac{5}{6})$  surface x-ray reflection vs. temperature, showing the full reversibility of the transition (heating up is represented with open circles and cooling down with solid circles).

The intensity for each point is obtained in this analysis integrating the fit of the angular scans, shown in panel d) of Fig. 2), to a Voigt line shape (in this case, the Gaussian contribution taking into account the experimental resolution was marginal). The diffraction peaks are measured along the phase transition in thermodynamic equilibrium. To this end, the temperature was slowly increased

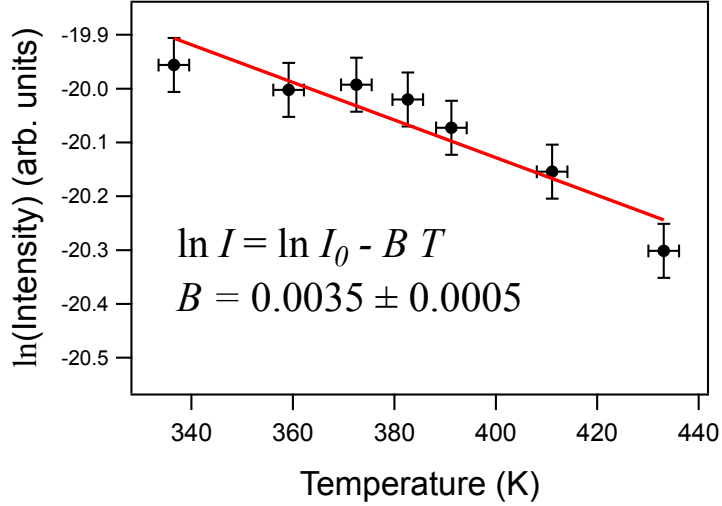


Figure 3: Linear fit (red line) of the logarithm of the integrated intensity of the x-ray reflection  $(\frac{1}{2}, \frac{1}{2})$  vs. temperature. The intensity decrease in this case is related only to the effect of thermal vibration through a DW factor ( $I = I_0 \exp^{-BT}$ ).

and the sample remained sufficient time at each temperature to reach equilibrium. The experiment was made both increasing and decreasing the temperature. In both cases the same curve was obtained, with an inflection point a 360 K, Fig. 2(e). We conclude that the phase transition proceeds without detectable hysteresis within the experimental accuracy. The lack of hysteresis and the continuous change of the peak intensity suggest that the phase transition is continuous.

The intensity is attenuated by the temperature through a Debye-Waller (DW) factor  $B$  ( $I = I_0 \exp^{-BT}$ ). The intensities used to study the phase transition have been corrected by the corresponding DW factor. The DW factor is estimated from the intensity reduction of a reflection not affected by the phase transition, see Fig.3. The value obtained for the DW factor is  $0.0035 \text{ K}^{-1}$ . The curve in Fig.2(c) shows the phase transition of the structural order parameter, with an inflection point at  $\sim 360 \text{ K}$ , the critical temperature of the phase transition, and without any distinguishable discontinuity.

### Detailed analysis of the critical behavior

In view of the behavior of the structural order parameter and the lack of hysteresis, the phase transition seems to be continuous. If we assume that the phase transition is of this type, we can



analyze the critical behavior applying Landau theory<sup>46</sup>. Relevant magnitudes change near the critical temperature  $T_c$  following a power law. It is convenient to introduce a reduced temperature  $\tau$ , which is defined as  $\tau \equiv \frac{T-T_c}{T_c}$ . Due to the loss of long range order (LRO) as temperature increases and approaches  $T_c$ , the intensity of the diffraction peak associated to the periodicity (structural order parameter) becomes zero with the following dependence for  $\tau < 0$ <sup>47</sup>:

$$I_{LRO} \propto |\tau|^{2\beta} \quad (1)$$

where  $\beta$  is the *critical exponent* in this case.

Near a continuous phase transition, the system is affected by fluctuations, due to the energetic equivalence of two or more configurations of the same symmetry, which will contribute to the same diffraction pattern. After cooling down slowly, one of them will be predominant, giving rise to a symmetry breaking. In real systems however, and due to the presence of steps and defects, these configurations give rise to coexisting extensive domains, one for each possible configuration, and all with the same average size and uniformly distributed across the surface. If we now heat the surface and approach again the critical temperature, in the area of each of these domains new subdomains will appear, corresponding to the structure of the other possible configurations, and whose size will increase as temperature approaches  $T_c$ , while their shape and position fluctuate with time. The average size of these subdomains is called correlation length  $\xi$ . This magnitude has a singularity right at  $T = T_c$ , which in real systems is simply a maximum, because the surface is not infinite and the growth cannot be unlimited. Above  $T_c$ , all the different domains fluctuate with the same probability and with decreasing correlation lengths. The critical behavior of  $\xi$  is described by the following power:

$$\xi \propto |\tau|^{-\nu} \quad (2)$$

As described above, the long range order (large single domain areas) disappears near  $T_c$  due to the divergent size growth of fluctuating domains near  $T_c$ . However, this fluctuations regime includes a short range order (SRO), with domains of size  $\xi$ , which contribute also to the intensity of a peak in

a diffraction experiment. Assuming an exponential distribution of domain sizes, the contribution to the diffraction intensity of the short range order is a Lorentzian:

$$F_{SRO}(q, T) = \frac{\chi(T)}{1 + q^2\xi^2(T)} \quad (3)$$

where  $q$  is the transferred parallel momentum and where the width is inversely proportional to the correlation length  $\xi$ . The height of the peak (susceptibility  $\chi$ ) follows also a power law, modelled with a new critical exponent  $\gamma$ :

$$\chi \propto |\tau|^{-\gamma} \quad (4)$$

In summary, the critical behavior of a diffraction peak affected by a phase transition contains the following contributions:

$$S(q, T) = I_{LRO}(T)F(q) + F_{SRO}(q, T) + I_{bg} \quad (5)$$

In this expression,  $I_{bg}$  is the background intensity,  $F(q)$  represents a convolution profile with a Gaussian due to the limited instrumental resolution (constant across the phase transition) and a Lorentzian, due to the finite size of the domains at low temperature. It is important to recall that  $S(q, T)$  is affected by a Debye-Waller factor and it should be multiplied by an exponential  $\exp^{-BT}$  taking into account the intensity reduction due to thermal vibrations, besides the intensity reduction due to the phase transition.

Fig. 4 shows the result of the fit made to determine the critical exponents of the phase transition in the system Sn/Cu(100). Panel d) shows three examples of the fit to the expression 5 of the x-ray reflection peak of order  $(\frac{5}{6}, \frac{5}{6})$  near a  $T_c$ , once the intensity is corrected by the DW factor  $\exp^{-0.0035T}$ . The green dotted curve corresponds to the fitted component of the SRO contribution, while the dashed blue curve is the fitted component of the LRO contribution. This fit is made leaving free the critical exponents  $\beta$ ,  $\nu$  and  $\gamma$  for each temperature. The factor  $F(q)$  of the expression 5 is of Voigt type, with a fixed Gaussian component of 0.0016 r.l.u. width. This value is obtained

after fitting the peaks measured at lowest temperature, whose width is narrowest and is limited by the experimental resolution. The Gaussian width used corresponds to an instrumental resolution of  $\sim 0.0028 \text{ \AA}^{-1}$ . The second component of the Voigt line shape is a Lorentzian, whose width is another free parameter in the fit. The value obtained for each critical exponent and each temperature is used to represent the temperature dependence  $I_{LRO}$ ,  $\chi$ , and  $\xi$  in panels a), b) and c) of Fig. 4. Note that a fit to all experimental points is not possible, as the behavior of the fit is not stable in the range near the phase transition. Only sufficiently far away from the phase transition, the fit converges consistently to one of the two components and then the results are meaningful. The same applies to the values of  $I_{LRO}$  above  $T_c$ , which are always compatible with zero, but not consistently reproducible. The following critical exponents are obtained from the fit of the experimental curves to the power laws described before:

$$\beta = 0.11 \pm 0.03$$

$$\gamma = 1.88 \pm 0.20$$

$$\nu = 0.89 \pm 0.25$$

## Data set

As in the case of the low temperature phase<sup>41</sup>, the data set was averaged using the  $p2mm$  symmetry group. A more restrictive group, like  $p4mm$ , would be compatible both with the LEED pattern observed and with the SXRD data set. However, the number of equivalent reflections using  $p4mm$  is not much higher than using  $p2mm$ , as the in-plane data set does not contain as many reflections as in the low temperature case. In order to make a comparison between the results for both phases easier, we chose to use the  $p2mm$  symmetry.

Fig. 5 shows all structure factors measured for the  $(\sqrt{2} \times \sqrt{2}) R45^\circ$  high temperature phase, classified as in-plane, crystal truncation rods and fractional rods. In-plane structure factors were measured for a perpendicular momentum transfer of  $l = 0.25$ . The 63 reflections measured were

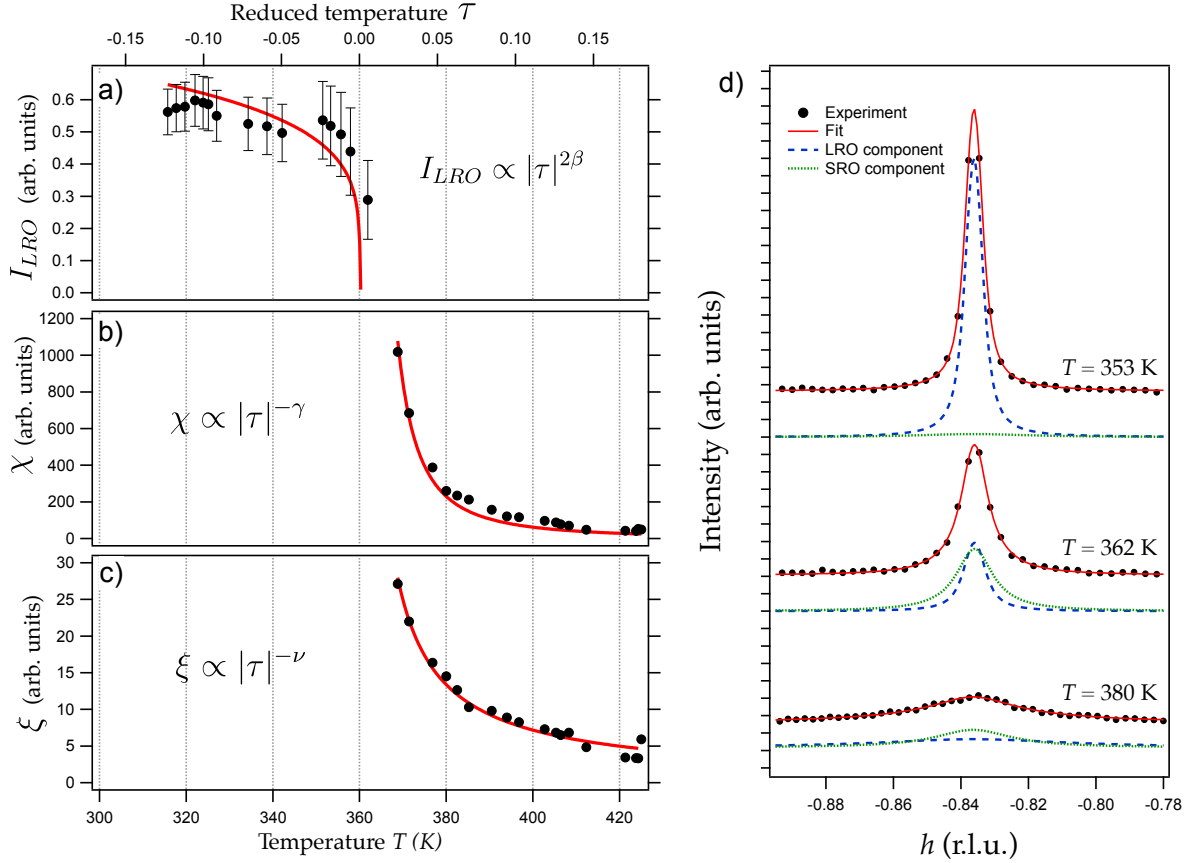


Figure 4: Panels a), b), and c): Temperature dependence of  $I_{LRO}$ ,  $\chi$ , and  $\xi$ , respectively. The red curves are a fit of the experimental data to the power laws with critical exponents  $\beta$ ,  $\gamma$ , and  $\nu$  (see text). The functions  $\chi$  and  $\xi$  diverge theoretically at  $T = T_c$ . In reality, there is no divergence due to finite size effects. Panel d): three examples of the fit of the diffraction peak at three different temperatures. The SRO component is negligible for  $T < T_c$  and the LRO component is negligible for  $T > T_c$ . For  $T \sim T_c$ , both components are comparable.

reduced by symmetry averaging to 24 non-equivalent reflections, according to the  $p2mm$  symmetry group. As the crystal truncation rods measured for  $(h, k) = (1, 0)$  and  $(0, -1)$  are equivalent, three non-equivalent CTRs were left. Four fractional rods belonging to the  $(\sqrt{2} \times \sqrt{2})$  R45° periodicity were measured as well. The agreement factor  $\epsilon$  (a measure of the systematic errors in the data set) is also shown in Fig. 5.

Fig. 6(a) shows the experimental Patterson diagram, obtained from the set of in-plane structure factors. It has been represented in an area three times larger than the unit cell for this phase, so that it can be easily compared to the Patterson diagram of the low temperature phase (Fig. 6 in Ref.

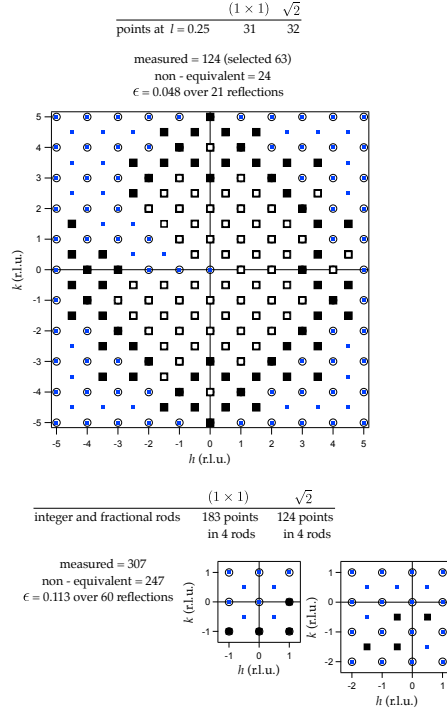


Figure 5:  $(1 \times 1)$  (circles) and  $(\sqrt{2} \times \sqrt{2})$   $R45^\circ$  (blue squares) reciprocal space points. Black squares mark experimental points measured for the high temperature phase. In-plane points finally selected are displayed as white squares (top panel). Non-equivalent points were obtained using the  $p2mm$  symmetry group. The mean value of the agreement factor (calculated for points with at least one equivalent reflection) is shown as well. The label  $\sqrt{2}$  denotes points belonging exclusively to the  $(\sqrt{2} \times \sqrt{2})$   $R45^\circ$  periodicity.

41). A visual inspection reveals that there cannot be too many changes in the atomic positions with respect to the low temperature phase.

## Structural model

In this section we analyze the surface structure of  $\text{Sn/Cu}(100)$ - $(\sqrt{2} \times \sqrt{2})R45^\circ$  using the genetic algorithm with the objective of understanding the properties of this phase and of the surface phase transition from  $(3\sqrt{2} \times \sqrt{2})$   $R45^\circ$  to  $(\sqrt{2} \times \sqrt{2})$   $R45^\circ$  at  $360 \text{ K}^{21}$ .

Fig. 7 shows that both crystal truncation rods (CTRs) and fractional rods  $(-\frac{1}{2}, \frac{1}{2})$  and  $(\frac{1}{2}, \frac{1}{2})$  measured for the high-temperature phase, change with perpendicular momentum  $l$  in the same way as the corresponding rods of the low-temperature phase (Fig. 8 in Ref. 41). This behavior suggests

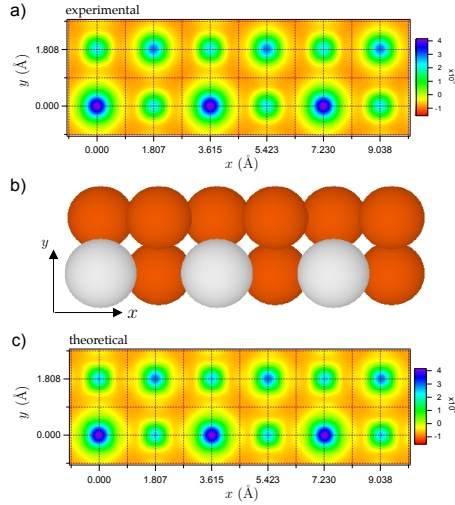


Figure 6: a) Experimental Patterson diagram obtained from the in-plane data set ( $l = 0.25$ ) of the high temperature ( $\sqrt{2} \times \sqrt{2}$ ) R45° phase. b) Top view of the surface unit cell obtained from the fit of the structural model. The unit cell is reproduced three times to facilitate the comparison with the ( $3\sqrt{2} \times \sqrt{2}$ ) R45° phase. c) Theoretical Patterson diagram calculated from the atomic positions shown in b).

that the local structure is substantially the same in both phases, and that the high-temperature phase is disordered. On the basis of this evidence, we have constructed a structural model that is compatible with the structure of the low-temperature phase and at the same time with the specific features of the high-temperature phase. The surface unit cell is three times smaller, as shown in Fig.8, where the disordered behavior of the high-temperature phase is simulated introducing two Sn atoms at the same adsorption site with slightly different heights, and with a different occupation parameter for each of them. As there are two different heights, this model can reproduce the two vertical displacements present in the low-temperature phase for Sn atoms. Following the model found before for the low-temperature phase<sup>41</sup>, the only Cu atom in the last layer has also an occupation parameter. Now the fitting is made keeping all the occupation parameters free during the whole fitting process, so that the model is as general as possible. Note that this model contains also ordered phases, so that depending on the value of the occupation parameters we may talk or not about a disordered phase. A non-disordered phase would be characterized by values of the occupation equal to 0 or 1. In summary, the model has a total number of 13 atoms in the surface unit cell, and 27 free parameters. As the full data set used to fit the data contains 271

non-equivalent structure factors (see Fig. 5), there is a safe ratio of  $\sim 10$  experimental structure factors per parameter. The 27 free parameters are the following:

- 3 non-structural parameters, related with scale factors and the  $\beta$  factor of surface roughness.
- 13 atomic displacements, corresponding to the vertical movements of each atom.
- 3 occupation parameters, one for each atom belonging to the last atomic layer. These parameters vary in the 0 to 1 range and represent the presence of one atom at the surface in mean value.
- 8 temperature parameters (4 in-plane and 4 out-of-plane, see Fig. 8). The two Sn atoms have the same temperature factor with different in-plane and out-of-plane values ( $B1$ ). The only last-layer Cu atom has an independent temperature factor ( $B2$ ), while atoms in the second layer were assigned a different temperature factor ( $B3$ ). The fourth factor was assigned to all additional atoms belonging to the 4 additional layers ( $B4$ ).

## Fit of the structural model

The process of refinement of the atomic positions and temperature factors of the structural model was conducted using the full set of experimental data (crystal truncation rods, fractional rods and in plane data) in all steps. The following sequence was used:

1. In the first fit, temperature factors were taken from the estimated values in Table 1 from Ref. 41. Also an estimated value of  $0.83 \text{ \AA}^2$  was taken for the isotropic temperature factor associated to the bulk unit cell<sup>41</sup>. Atomic displacements were left free, with initial values equal to 0, except for the three atoms in the top layer, which were assigned the atomic positions of the corresponding atoms in the low temperature unit cell as starting values. The range of allowed variation was  $0.2 \text{ \AA}$ , and the occupation parameters could vary in the whole range (from 0 to 1), with an initial value of 0.5.

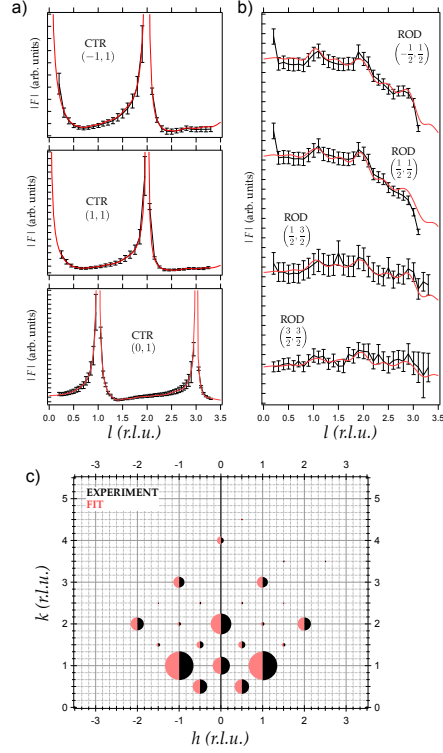


Figure 7: a) Non-equivalent crystal truncation rods of the  $(\sqrt{2} \times \sqrt{2})R45^\circ$  phase. b) Fractional rods. Black dots are experimental points with their error bars. The red curve is calculated from the fitted structural model. c) Non-equivalent in-plane reflections (measured for  $l = 0.25$ ). The radius of each half-circle is proportional to the measured structure factor (black) and the structure factor calculated with the fitted structural model (red).

2. After the fit in point 1, the atomic heights of last layer atoms converged to values almost identical to the final ones. However, the occupation parameters found were:  $O_A = 14\%$ ,  $O_B = 60\%$ , and  $O_C = 56\%$ , which are significantly different from the final values obtained including the temperature factors. This feature suggests that temperature factors are crucial now for the fit. The  $R$ -factor reached was  $0.5\%$ , corresponding to a  $\chi^2=3.36$ , still much larger than the final value obtained.
3. A last fit was made using the results of the previous fit as starting values, and leaving all parameters free, including temperature factors. The value of each temperature factor could vary between  $0$  and  $6 \text{ \AA}^2$ . After all parameters converged within their range, the  $R$ -factor value was  $0.21\%$ , corresponding to a  $\chi^2$  of  $0.87$ .



Fig.7 shows all data used for the fit. The data are compared to the calculated structure factors, obtained for the optimized structural model. The agreement is excellent in all cases. A Patterson diagram obtained using the calculated structure factors of the optimized structural model is shown in Fig. 6(c). It coincides very accurately with the Patterson diagram obtained from the experimental structure factors, Fig.6(a).

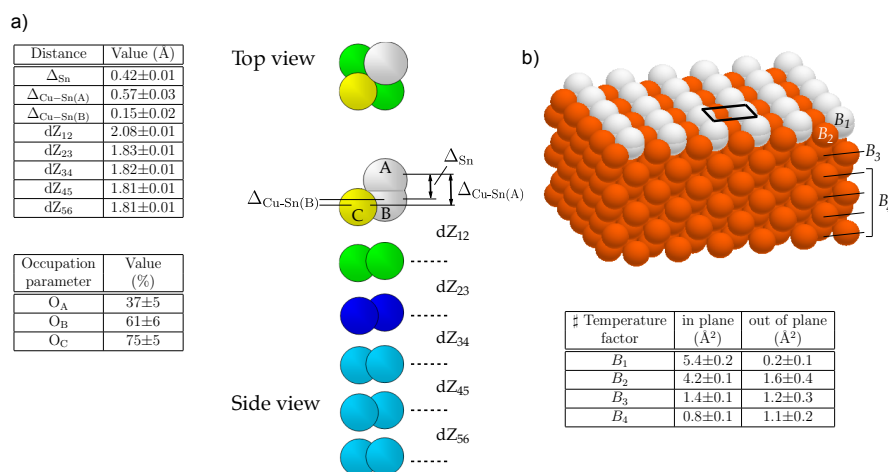


Figure 8: a) Main distances (in Å) obtained from the fit of the  $(\sqrt{2} \times \sqrt{2})$   $R45^\circ$  high temperature phase. The atomic positions are represented on panel (b) in an exaggerated scale to better show the relative positions within each layer. Distances between layers are referred to the centre of mass of each layer. Occupation parameters are assigned to each of the three atoms of the last atomic layer. The values obtained in the fit are shown in the Table. b) Three-dimensional perspective view of the unit cell repeated thirty times, using the real positions obtained from the fit. A square marks the surface unit cell. The Table collects the values of the temperature factors (see text).

## Description of the structural model

Fig.8 shows the final atomic configuration of the structural model found, together with the main atomic distances calculated from the fitted parameters, and the temperature factors. The model found presents several interesting features.

1-The two Sn atoms in the unit cell, which are initially at the same height, are separated by a vertical distance of  $0.42 \text{ \AA}$ . As it is physically very improbable that two Sn atoms are so close to each other, the occupation parameters  $O_A$  and  $O_B$  should be interpreted as average presence of each of these two atoms<sup>48</sup>, i.e. we can find surface unit cells with a Sn atom at a higher level, and

surface unit cells with a Sn atom at a lower level. The relative abundance of each of these sites [see Table a) in Fig.8(a)] coincides within accuracy with the fraction of Sn atoms at each height in the low temperature phase (one out of three Sn atoms in the unit cell is higher than the other two, i.e. 33.3 % and 66.6% respectively).

2-The low temperature phase is characterized by a missing Cu row in the last atomic layer, so that the Cu atomic sites in this layer are 66.6% occupied. However, the outcome of the fit for the high temperature phase corresponds to an occupation of  $O_C = 75 \pm 5 \%$ . In order to rationalize this change, let us consider the probability of finding 0, 1, 2, 3 or 4 Cu atoms around a Sn atom (see Fig.9), i.e. in the four nearest neighbor sites. If  $O_C$  is the probability of finding a particular Cu site occupied, each of the 5 possibilities exhibits a probability of being observed  $P_i$ , whose values can be easily obtained, assuming no correlation between neighboring Sn or Cu atoms. The probabilities are:

$$P_0 = (1 - O_C)^4$$

$$P_1 = 4 \cdot (1 - O_C)^3 \cdot O_C$$

$$P_2 = 6 \cdot (1 - O_C)^2 \cdot O_C^2$$

$$P_3 = 4 \cdot (1 - O_C) \cdot O_C^3$$

$$P_4 = O_C^4$$

The values  $O_A = 37 \pm 5\%$  and  $O_B = 61 \pm 6\%$  agree within accuracy with the corresponding occupations in the low temperature phase, and support that the fraction of Sn atoms with each height remains constant across the phase transition. Sn atoms present a high position in the low temperature phase when the four nearest neighbor sites are occupied by Cu atoms. This configuration has a  $P_4$  probability in the random phase model described. As both phases should be compatible

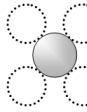
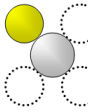
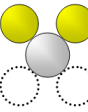
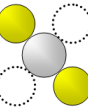
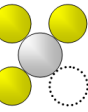
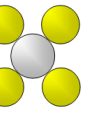
	$P_0$	$P_1$	$P_2$		$P_3$	$P_4$
Unequivalent configurations						
Variations	1	4	4	2	4	1
Probability	0.0033	0.0421	0.1332	0.0666	0.4214	0.3333

Figure 9: Schematic representation of the possible atomic configurations of last-layer atoms in the disorder model proposed for the high temperature phase. Each of the four atomic positions around the Sn atom can be occupied by a Cu atom with a probability  $(\frac{1}{3})^{\frac{1}{4}} = 0.7598$  so that  $P_4$  is  $\frac{1}{3}$  (see text). Based on this value, the remaining configurations have an associated probability shown in the last row of the table.

regarding the presence of Sn atoms at each height,  $P_4 = \frac{1}{3}$ , so that

$$O_C^4 = \frac{1}{3}, \text{ and then } O_C = \left(\frac{1}{3}\right)^{\frac{1}{4}} \simeq 0.7598$$

This value coincides with the occupation obtained from the fit. However, we have assumed that having occupied all nearest neighbor sites of a Sn atom is the only configuration shown in Fig. 9 where the Sn atom is at a higher level. Including any other configuration prevents reproducing the  $O_C$  value obtained from the fit. For instance, if the Sn atom could be at a higher level also when three neighbor sites are occupied, the predicted value for  $O_C$  would be obtained by solving the equation:

$$P_3 + P_4 = 4 \cdot (1 - O_C) \cdot O_C^3 + O_C^4 = \frac{1}{3}$$

The solution is  $O_C = 0.5137$ . As this value differs significantly from the value obtained from the experimental data, we conclude that the only possibility for having a Sn atom at a higher level is that its four nearest neighbor sites are occupied, as in the low temperature phase.

3-The total temperature factor (obtained by adding the in plane and out of plane factors) of each type of atom is in general larger than the values found for the  $(3\sqrt{2} \times \sqrt{2})$  R45° low temperature phase, as expected ( $\sim 5.7 \text{ \AA}^2$  vs.  $\sim 4.5 \text{ \AA}^{241}$  for the last layer,  $\sim 2.6 \text{ \AA}^2$  vs.  $\sim 1.5 \text{ \AA}^{241}$  for the

last but one layer and  $\sim 1.9 \text{ \AA}^2$  vs.  $\sim 0.9 \text{ \AA}^2$  for all other layers). We note that the out of plane temperature factor related to Sn atoms is very small, probably because the model permits two equilibrium positions, each with its own occupation, instead of a single vibrating atom. The in plane temperature factor ( $5.4^2$ ) corresponds to a mean oscillation amplitude of  $\sqrt{\frac{5.4}{8\pi^2}} = 0.26 \text{ \AA}$ , a value close to the lateral displacement obtained in the low temperature phase for the Sn atoms that get closer to each other ( $0.27 \text{ \AA}$ ). We may interpret these results considering that the fit of the  $(\sqrt{2} \times \sqrt{2}) \text{ R}45^\circ$  high temperature results does not permit lateral displacements, due to symmetry reasons. This feature is compensated by a larger in plane temperature factor.

## Discussion

The critical behavior of the structural phase transition  $(3\sqrt{2} \times \sqrt{2}) \text{ R}45^\circ \leftrightarrow (\sqrt{2} \times \sqrt{2}) \text{ R}45^\circ$  observed for a coverage 0.5 ML of Sn on Cu(001) has been analyzed in detail. The evolution of the  $(\frac{5}{6}, \frac{5}{6})$  reflection is measured as a function of temperature. Each peak is fit to a theoretical line shape describing the behavior of the critical dispersion of the phase domains at the surface. The lack of hysteresis and the gradual decrease of the order parameter with temperature suggest that the phase transition is continuous. Assuming this assignment, the critical exponents are obtained from the previous analysis. The experimental critical exponents are compatible with the theoretical values calculated for the Ising 2D model ( $\beta = \frac{1}{8}$ ,  $\gamma = \frac{7}{4}$  y  $\nu = 1$ ), and thus the phase transition can be ascribed to the Ising 2D universality class. In the case of superstructures formed by adsorbates at surfaces, a lattice gas model Hamiltonian is frequently used. In this model it is assumed that the adsorbate remains at the same adsorption site along the transition and it is completely characterized by its position at the surface lattice. In this model, the application of Landau rules and of commensurability Lifshitz rules allows us to predict which superstructures can become the ordered phase of a certain order-disorder continuous phase transition in two dimensions<sup>49-51</sup>. For a detailed review on this matter we refer the reader to Refs. 52,53. In the case of the Sn/Cu(100) phase transition, and assuming that a lattice gas Hamiltonian can be applied, the high tempera-

ture square lattice found at high temperature [periodicity  $(\sqrt{2} \times \sqrt{2}) R45^\circ$ ], can only transit in a continuous way to phases with periodicity  $(4\sqrt{2} \times 4\sqrt{2}) R45^\circ$ ,  $(4\sqrt{2} \times 2\sqrt{2}) R45^\circ$  or  $p(2 \times 2)$ . Out of these phases, only the last one would exhibit a critical behavior belonging to the Ising 2D universality class. Any transition to other superstructure would be discontinuous (first order). The low temperature phase that we are considering has a periodicity  $(3\sqrt{2} \times \sqrt{2}) R45^\circ$ , which does not coincide with any of the previous ones. However, the lack of hysteresis and the continuous change of the order parameter along the phase transition do not support that the phase transition is discontinuous, within the limits of experimental resolution. Nevertheless, the existence of these features of discontinuous phase transitions can be suppressed by finite size effects or may be not easy to observe, in case the discontinuity is very small. On the other hand, a fluctuations regime as the one observed here is theoretically possible in discontinuous phase transitions with critical exponents determined by the system dimensionality<sup>54,55</sup>. This possibility can be discarded, because the experimental values obtained differ from the theoretical predictions in this case ( $\beta = 0$ ,  $\gamma = 1$ ,  $\nu = \frac{1}{2}$ ). The discrepancy in  $\beta$  (0.11 vs. 0) could be explained assuming that this values is strongly affected by the DW correction used in the delicate data fitting. On the contrary, the disagreement in  $\gamma$  (1.88 vs. 1) is not justified. The conclusion is that the critical behavior is not compatible with a discontinuous phase transition. This conclusion does not mean that the Landau theory is not correct in this case. On the one hand, the experimental resolution may be insufficient to discern an hypothetic symmetry in the phases, distinct from the symmetries experimentally observed by LEED and SXRD. This hidden order could be then compatible with Landau-Lifshitz rules and the phase transition would be continuous, belonging to the Ising 2D universality class, in view of the critical exponents. But even if this is not the case, it is necessary to describe the interactions at the surface with a proper Hamiltonian, different from the one used in the lattice gas model. The phenomenology described in the following for Sn/Cu(001) is more complex than the one assumed in this model, due for instance to the fact that the number of atoms at the surface is different for each phase (high and low temperature). It is obvious that the phase transition is not taking place exclusively at the surface, but it is affected by the diffusion of bulk atoms.

In fact, the disorder model proposed for the high temperature phase (as shown from the crystallographic data analysis) is not compatible with a lattice gas model, and the interactions at the interface should be described with a proper Hamiltonian to find out whether the phase transition can be continuous or not within the framework of Landau theory.

In the case of the high temperature phase, as the unit cell is three times smaller, the fit is made using occupation parameters of the last layer atoms. This is a more general model, able to reproduce a disordered behavior. This possibility is suggested by the obvious high degree of coincidence between diffraction rods of the high temperature and low temperature phases, revealing that the local structure should remain essentially identical at both temperatures. The best fit of the experimental data supports the conclusion that the high temperature phase ( $\sqrt{2} \times \sqrt{2}$ ) R45° is disordered. The disordering is characterized by an incoherent oscillation of the Sn atoms in vertical direction and the appearance and disappearance of Cu atoms at the adsorption sites around each Sn atom. The physical mechanism leading to this diffusion of Cu atoms into the top atomic layer cannot be determined directly from the SXRD data. We can only estimate that the number of Cu atoms involved in this process is 14% larger than in the low temperature phase. The excess Cu atoms could come from steps or from the bulk. The variation of the Cu atomic density in the last atomic layer involves a change in the number of particles and thus an influence on the chemical potential. This feature is not taken into account by the lattice gas model, but it should be considered for a proper application of Landau theory in order to determine whether a continuous phase transition is possible. Time-of-flight direct-recoil spectroscopy results found that the number of detectable Cu atoms that have an atom vacancy in the next-neighbor site along the beam direction is approximately constant across the phase transition<sup>28</sup>, while in the case of totally disordered vacancies a 33% increase would be expected. The increase in the number of Cu atoms could explain this apparent inconsistency, although other explanation was proposed by Gayone and co-workers<sup>28</sup>, and more experiments would be required to solve this point.

STM images are compatible with the models optimized from the crystallographic analysis. In the case of the low temperature phase, the bright atoms seen with STM are identified with

Sn atoms of the structural model. However, it is not possible to confirm the lack of one out of three Cu rows in the last atomic layer, as shown with high certitude by the crystallographic analysis. The Cu diffusion proposed for the high temperature phase, which is behind the disordered behavior, explains the lack of long range order, but the disordering is a very fast process and STM images only register the time average. Thus, the observed unit cell is square and corresponds to a  $(\sqrt{2} \times \sqrt{2}) R45^\circ$  periodicity.

## Conclusion

The structural model obtained for the HT phase consistently supports a description of this phase as disordered, with Sn atoms oscillating between two different heights along the surface normal. The actual height of a particular Sn atom depends on the number of nearest Cu neighbors in the layer underneath. The disorder mechanism is determined by the diffusion of these Cu atoms through vacancies in this layer. The ordering of vacancies gives rise to the missing Cu rows, typical of the low-temperature phase. The fraction of Cu atoms in the last layer corresponds to 0.75 atoms of Cu by each Sn atom, vs. 0.66 in the LT phase. This represents an increase of 14% in the number of Cu atoms in the last layer, indicating that the number of vacancies in equilibrium changes upon crossing the phase transition.

## Acknowledgement

This work was funded by the Spanish MINECO under grants FIS2011-23230 and MAT2014-52477-C5-5-P. E.G.M. and P.S. acknowledge financial support from MINECO through the “María de Maeztu” Programme for Units of Excellence in R&D (MDM-2014-0377). The authors thank X. Torrelles and J.A. Martin-Gago for fruitful discussions and the E.S.R.F. staff for help and support.

## References

- (1) Binder, K. In *Phase Transitions and Critical Phenomena*; Domb, C., Lebowitz, J., Eds.; Academic, 1983; Vol. 8; pp 2–145.
- (2) Diehl, H. In *Phase Transitions and Critical Phenomena*; Domb, C., Lebowitz, J., Eds.; 1986; Vol. 10; pp 76–269.
- (3) Mills, D. L. Surface Effects in Magnetic Crystals near the Ordering Temperature. *Phys. Rev. B* **1971**, *3*, 3887–3895.
- (4) Frenken, J. W. M.; Veen, J. F. v. d. Observation of Surface Melting. *Phys. Rev. Lett.* **1985**, *54*, 134–137.
- (5) Erwin, S. C.; Baski, A. A.; Whitman, L. J.; Rudd, R. E. Frenkel-Kontorova Model of Vacancy-Line Interactions on Ga /Si(112). *Phys. Rev. Lett.* **1999**, *83*, 1818–1821.
- (6) Voigtländer, B. Fundamental Processes in Si/Si and Ge/Si Epitaxy Studied by Scanning Tunneling Microscopy during Growth. *Surf. Sci. Rep.* **2001**, *43*, 127 – 254.
- (7) Snijders, P. C.; Moon, E. J.; González, C.; Rogge, S.; Ortega, J.; Flores, F.; Weitering, H. H. Controlled Self-Organization of Atom Vacancies in Monatomic Gallium Layers. *Phys. Rev. Lett.* **2007**, *99*, 116102.
- (8) Tamura, K.; Mizuki, J. Structural Kinetics Studies on Phase Transitions of the Bi UPD Layer between the  $(2 \times 2)$  and  $(p \times \sqrt{3})$  Structures Using Surface X-ray Diffraction. *J. Phys. Chem. B* **2005**, *109*, 12832–12836.
- (9) Zhang, L.; Yang, Y.; Huang, H.; Lyu, L.; Zhang, H.; Cao, N.; Xie, H.; Gao, X.; Niu, D.; Gao, Y. Thickness-Dependent Air-Exposure-Induced Phase Transition of CuPc Ultrathin Films to Well-Ordered One-Dimensional Nanocrystals on Layered Substrates. *J. Phys. Chem. C* **2015**, *119*, 4217–4223.



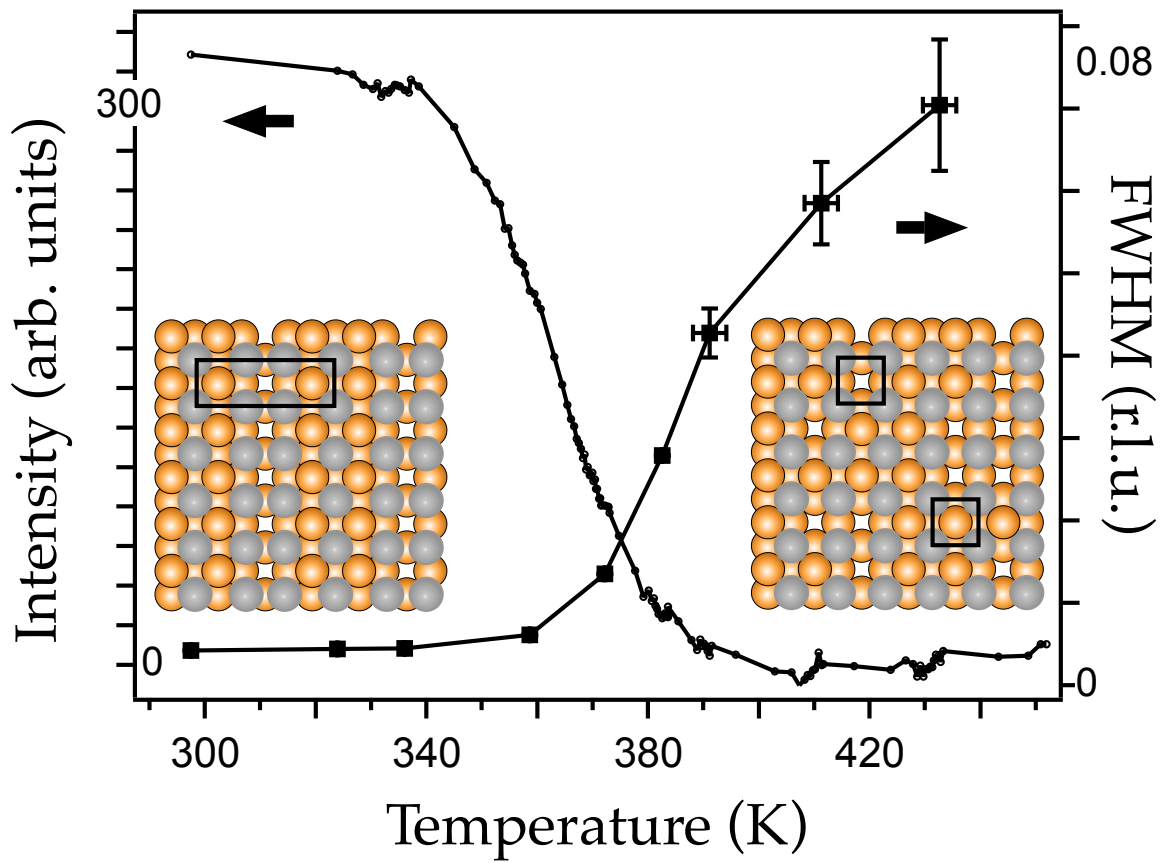
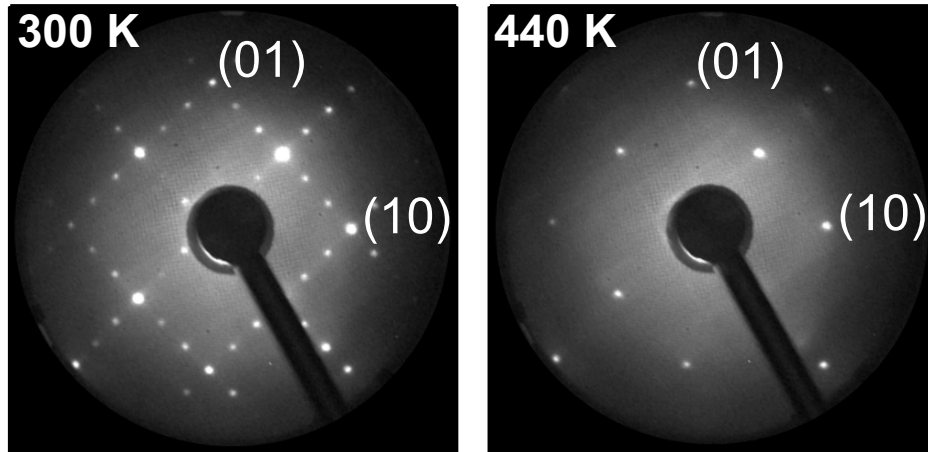
- (10) Lucas, C. A.; Maroun, F.; Sisson, N.; Thompson, P.; Gründer, Y.; Cortès, R.; Allongue, P. Film and Interface Atomic Structures of Electrodeposited Co/Au(111) Layers: An in Situ X-ray Scattering Study as a Function of the Surface Chemistry and the Electrochemical Potential. *J. Phys. Chem. C* **2016**, *120*, 3360–3370.
- (11) P. A. Dowben, M. D., Nolting, W., Eds. *Magnetism and electronic correlations in local-moment systems: Rare-earth elements and compounds*; World Scientific, 1998; Chapter 7.
- (12) Cortés, R.; Tejada, A.; Lobo-Checa, J.; Didiot, C.; Kierren, B.; Malterre, D.; Merino, J.; Flores, F.; Michel, E. G.; Mascaraque, A. Competing Charge Ordering and Mott Phases in a Correlated Sn/Ge(111) Two-Dimensional Triangular Lattice. *Phys. Rev. B* **2013**, *88*, 125113.
- (13) Diguet, G.; Hearne, G. R.; Sibanda, W. N.; Carleschi, E.; Musyimi, P.; Pischedda, V.; Attfield, J. P. Wigner-Mott Insulator-to-Insulator Transition at Pressure in Charge-Ordered Fe<sub>2</sub>OBO<sub>3</sub>. *Phys. Rev. B* **2014**, *89*, 035132.
- (14) Qin, S.; Kim, J.; Niu, Q.; Shih, C.-K. Superconductivity at the Two-Dimensional Limit. *Science* **2009**, *324*, 1314–1317.
- (15) Richter, C.; Boschker, H.; Dietsche, W.; Fillis-Tsirakis, E.; Jany, R.; Loder, F.; Kourkoutis, L. F.; Muller, D. A.; Kirtley, J. R.; Schneider, C. W. et al. Interface superconductor with gap behaviour like a high-temperature superconductor. *Nature* **2013**, *502*, 528–531.
- (16) Tosatti, E. In *Electronic Surface and Interface States on Metallic Systems*; Bertel, E., Donath, M., Eds.; World Scientific, 1994; pp 67–89.
- (17) Mascaraque, A.; Michel, E. Reversible Structural Phase Transitions in Semiconductor and Metal/Semiconductor Surfaces. *J. Phys.: Condens. Matter* **2002**, *14*, 6005–6035.
- (18) Swamy, K.; Menzel, A.; Beer, R.; Bertel, E. Charge-Density Waves in Self-Assembled Halogen-Bridged Metal Chains. *Phys. Rev. Lett.* **2001**, *86*, 1299–1302.

- (19) Yeom, H.; Takeda, S.; Rotenberg, E.; Matsuda, I.; Horikoshi, K.; Schaefer, J.; Lee, C.; Kevan, S.; Ohta, T.; Nagao, T. et al. Instability and Charge Density Wave of Metallic Quantum Chains on a Silicon Surface. *Phys. Rev. Lett.* **1999**, *82*, 4898–4901.
- (20) Nakagawa, T.; Boishin, G.; Fujioka, H.; Yeom, H.; Matsuda, I.; Takagi, N.; Nishijima, M.; Aruga, T. Fermi Surface Nesting and Structural Transition on a Metal Surface: In/Cu (001). *Phys. Rev. Lett.* **2001**, *86*, 854–857.
- (21) Martínez-Blanco, J.; Joco, V.; Ascolani, H.; Tejada, A.; Quirós, C.; Panaccione, G.; Balasubramanian, T.; Segovia, P.; Michel, E. Fermi Surface Gapping and Nesting in the Surface Phase Transition of Sn/Cu(100). *Phys. Rev. B* **2005**, *72*, 041401(R).
- (22) Binns, C.; Barthes-Labrousse, M.; Norris, C. Charge Density Waves in Quasi-One-Dimensional Thallium Overlayers. *Journal of Physics C* **1984**, *17*, 1465–1472.
- (23) Delamare, F.; Rhead, G. First Stages of Deposition of Bismuth on Copper Examined by LEED. 1.(100) substrate. *Surf. Sci.* **1973**, *35*, 172–184.
- (24) Meyerheim, H.; De Santis, M.; Moritz, W.; Robinson, I. Domain-Wall Interactions in Bi/Cu(001). *Surf. Sci.* **1998**, *418*, 295–302.
- (25) Joco, V.; Martínez-Blanco, J.; Segovia, P.; Vobornik, I.; Michel, E. G. Surface Electronic Structure of Pb/Cu(100): Surface Band Filling and Folding. *J. Phys.: Condens. Matter* **2009**, *21*, 474216.
- (26) Aruga, T. Charge-Density Waves on Metal Surfaces. *J. Phys.: Condens. Matter* **2002**, *14*, 8393–8414.
- (27) Aruga, T. Surface Peierls Transition on Cu(001) Covered with Heavier p-Block Metals. *Surf. Sci. Reports* **2006**, *61*, 283–302.
- (28) Gayone, J. E.; Carrera, A.; Grizzi, O.; Bengio, S.; Sanchez, E. A.; Martinez-Blanco, J.;

- Michel, E. G.; Fuhr, J. D.; Ascolani, H. Order-Disorder Phase Transition of Vacancies in Surfaces: The Case of Sn/Cu(001)-0.5 ML. *Phys. Rev. B* **2010**, *82*, 035420.
- (29) Rhead, G.; Argile, C.; Barthes, M. Quantitative Auger Electron Spectroscopy of Metal Monolayers on Metals. *Surf. Interface Anal.* **1981**, *3*, 165–172.
- (30) Argile, C.; Rhead, G. Growth of Metal Monolayers and Ultrathin Films on Copper: Simple and Bimetallic Layers of Lead and Tin. *Thin Solid Films* **1982**, *87*, 265–275.
- (31) Argile, C.; Rhead, G. Surface Alloy Formation in Ultrathin Layers and Bimetallic Double Monolayers: Tin and Lead on Copper(100) and Copper(111). *Surf. Sci.* **1983**, *135*, 18–34.
- (32) McLoughlin, E.; A.A., C.; E., A.; C.J., B. A Re-Interpretation of the Cu{100}/Sn Surface Phase Diagram. *Surf. Sci.* **2001**, *482-485*, 1431–1439.
- (33) Pussi, K.; AlShamaileh, E.; McLoughlin, E.; Cafolla, A.; Lindroos, M. Determination of the structure of Cu{100}-p( $3\sqrt{2} \times \sqrt{2}$ ) R45°-Sn by dynamical LEED. *Surf. Sci.* **2004**, *549*, 24–30.
- (34) Martínez-Blanco, J.; Joco, V.; Segovia, P.; Balasubramanian, T.; Michel, E. Surface Phase Diagram and Temperature Induced Phase Transitions of Sn/Cu(100). *Appl. Surf. Sci.* **2006**, *252*, 5331–5334.
- (35) Nara, Y.; Yaji, K.; Iimori, T.; Nakatsuji, K.; Komori, F. STM Observation of Surface Phases of Sn/Cu(001). *Surf. Sci.* **2007**, *601*, 5170–5172.
- (36) Lallo, J.; Goncharova, L.; Hinch, B.; Rangan, S.; Bartynski, R.; Strongin, D. Structural Studies of Sub Monolayer Sn/Cu(001) Structures. *Surf. Sci.* **2008**, *602*, 2348.
- (37) Martínez-Blanco, J.; Joco, V.; Fujii, J.; Segovia, P.; Michel, E. Electronic Structure and Fermi surface of Sn/Cu(001)-( $3\sqrt{2} \times \sqrt{2}$ ) R45°. *Phys. Rev. B* **2008**, *77*, 195418.

- (38) Nakagawa, T.; Okuyama, H.; Nishijima, M.; Aruga, T.; Yeom, H.; Rotenberg, E.; Krenzer, B.; Kevan, S. Dual Nature of a Charge-Density-Wave Transition on In/Cu(001). *Phys. Rev. B* **2003**, *67*, 241401.
- (39) Martinez-Blanco, J.; Joco, V.; Fujii, J.; Segovia, P.; Michel, E. G. Electronic Structure of Sn/Cu(100)- $(2\sqrt{2} \times 2\sqrt{2})R45^\circ$ . *J. Phys.: Condens. Matter* **2009**, *21*, 055001.
- (40) Yaji, K.; Nara, Y.; Nakatsuji, K.; Iimori, T.; Yagyu, K.; Nakayama, R.; Nemoto, N.; Komori, F. Phase Transition and Electronic State Modification by Lattice Strain in 0.5-Monolayer Sn/Cu(001). *Phys. Rev. B* **2008**, *78*, 035427.
- (41) Martinez-Blanco, J.; Joco, V.; Quiros, C.; Segovia, P.; Michel, E. G. Surface X-Ray Diffraction Analysis Using a Genetic Algorithm: the Case of Sn/Cu(100)- $(3\sqrt{2} \times \sqrt{2})R45^\circ$ . *J. Phys.: Condens. Matter* **2009**, *21*, 134011.
- (42) Walker, M.; Brown, M.; Draxler, M.; Dowsett, M.; McConville, C.; Noakes, T.; Bailey, P. Structural Analysis of the Cu(100)- $p(3\sqrt{2} \times \sqrt{2})R45^\circ$ -Sn Surface using Low and Medium Energy Ion Scattering Spectroscopies. *Surface Science* **2011**, *605*, 1934 – 1940.
- (43) Fuhr, J. D.; Gayone, J. E.; Martinez-Blanco, J.; Michel, E. G.; Ascolani, H. Structural and Electronic Properties of  $(3\sqrt{2} \times \sqrt{2})R45^\circ$ -Sn/Cu(100): Density functional theory and scanning tunneling microscopy. *Phys. Rev. B* **2009**, *80*, 115410.
- (44) Dutta, P.; Sinha, S. Analytic Form for the Static Structure Factor for a Finite Two-Dimensional Harmonic Lattice. *Phys. Rev. Lett.* **1981**, *47*, 50–53.
- (45) Vlieg, E. ROD: A program for Surface X-Ray Crystallography. *Journal of Applied Crystallography* **2000**, *33*, 401–405.
- (46) Landau, L.; Lishitz, E. *Statistical Physics*; Course of Theoretical Physics; Pergamon Press, 1958; Vol. 5.

- (47) Roelofs, L.; Kortan, A.; Einstein, T.; Park, R. Critical Exponents of a Four-State Potts Chemisorbed Overlayer:  $p(2 \times 2)$  Oxygen on Ni(111). *Phys. Rev. Lett.* **1981**, *46*, 1465–1468.
- (48) Meyerheim, H.; Sawitzki, R.; Moritz, W. X-ray Structure Analysis on Alkali Metals Adsorbed on Ge(001)( $2 \times 1$ ). *Phys. Rev. B* **1995**, *52*, 16830–16844.
- (49) Domany, E.; Schick, M.; Walker, J. Classification of Order-Disorder Transitions in Common Adsorbed Systems: Realization of the Four-State Potts Model. *Phys. Rev. Lett.* **1977**, *38*, 1148–1151.
- (50) Domany, E.; Schick, M.; Walker, J.; Griffiths, R. Classification of Continuous Order-Disorder Transitions in Adsorbed Monolayers. *Phys. Rev. B* **1978**, *18*, 2209–2217.
- (51) Rottman, C. Symmetry Classification of Continuous Phase Transitions in Two Dimensions. *Phys. Rev. B* **1981**, *24*, 1482–1492.
- (52) Schick, M. The Classification of Order–Disorder Transitions on Surfaces. *Prog. Surf. Sci.* **1981**, *11*, 245–292.
- (53) Persson, B. Ordered Structures and Phase Transitions in Adsorbed Layers. *Surf. Sci. Reports* **1992**, *15*, 1–135.
- (54) Fisher, M.; Berker, A. Scaling for First-Order Phase Transitions in Thermodynamic and Finite Systems. *Phys. Rev. B* **1982**, *26*, 2507–2513.
- (55) Challa, M.; Landau, D.; Binder, K. Finite-Size Effects at Temperature-Driven First-Order Transitions. *Phys. Rev. B* **1986**, *34*, 1841–1852.



TOC graphic